Arabian Journal of Geosciences (2021) 14: 2593
https://doi.org/10.1007/s12517-021-08877-4

ORIGINAL PAPER

# Theoretical and experimental study on the local head loss effect of complex rock fracture networks

**Zihao Niu[1] · Zhende Zhu[1] · Cheng Liu[1] · Xiangcheng Que[1] · Xinghua Xie[2]**

Received: 29 April 2021 / Accepted: 8 November 2021 / Published online: 23 November 2021


**Abstract**
Research on the seepage characteristics of rock fracture networks remains a challenge in hydraulic engineering design and construction. In order to establish a theoretical model that can describe the seepage characteristics of complex fracture network, based on the equivalent seepage resistance model, considering the local pressure drop loss effect at the intersection of fractures, and the equivalent local loss resistance model (E-loss model) is established. To verify the applicability of the theoretical model, two kinds of quadrilateral and hexagonal columnar jointed rock mass fracture networks are established with transparent polymethyl methacrylate (PMMA) plates as test objects. Through physical model tests, the influence of the water pressure drop conditions on fracture flow is explored. The results indicate that the theoretical model suitably reflects the experimental results under laminar flow conditions at a low Reynolds number. General-purpose computational fluid dynamics (CFD) code FLUENT is applied to analyze the mesoscale flow state in the fracture network, and the internal streamline and velocity vector characteristics are obtained. The results show that with the sudden decrease of fracture width in the fracture network, there is an obvious eddy current blocking effect, which is consistent with the analysis results of the theoretical model.

**Keywords** Fracture network · Seepage characteristics · Seepage resistance · Equivalent local loss resistance · Model test · CFD

## Introduction

Understanding the hydraulic characteristics of fractured rock masses plays an important role in oil exploitation, hydropower engineering, pollutant control engineering, etc. (Qian et al. 2011; Wang et al. 2015; Chen et al. 2016; Qiao et al. 2017; Li et al. 2020). The fracture network in a given rock mass is very complex, and its seepage characteristics are directly related to numerous factors. In fractured rock masses, the permeability of the intact rock masses is usually very low, and the fracture network provides the main channels of fluid flow (Su et al. 1999; Cherubini et al. 2012; Wang et al. 2013; Yang et al. 2014). It is reasonable to assume that the fracture aperture and connection form are related to the flow characteristics of the fluid occurring in the fracture. In related research, appropriate analysis of fracture network flow at the laboratory scale constitutes the basis of understanding flow through a real complex fracture rock mass network (Baghbanan and Jing, 2007; Takahashi et al. 2013; Wang et al. 2014; Shang et al. 2019).

Communicated by Broder J. Merkel.

Cheng Liu
njliucheng@hhu.edu.cn

Zihao Niu
hhuniuzihao@hhu.edu.cn

Zhende Zhu
zzdnj@hhu.edu.cn

Xiangcheng Que
qxc1129@hhu.edu.cn

Xinghua Xie
xiexh@nhri.cn

1 Key Laboratory of Ministry of Education for Geomechanics and Embankment Engineering, Jiangsu Research Center for Geotechnical Engineering Technology, Hohai University, Nanjing 210098, China

2 State Key Laboratory of Hydrology Water Resources and Hydraulic Engineering, Nanjing Hydraulic Research Institute, Nanjing 210098, China

The basic forms of fracture networks include single fractures and cross fractures. Different scholars have performed much research on single-fracture seepage through theoretical analysis, numerical calculation, and experimental exploration (Lomize, 1951; Louis 1969; Skjetne et al. 1999; Berkowitz 2002; Scesi and Gattinoni 2007). In regard to fracture seepage, when the Reynolds number is low, the flow and pressure gradient generally conform to the linear cubic law; with increasing Reynolds number, the flow rate and pressure gradient gradually deviate from the linear relationship, and the resultant nonlinear characteristics can be described with the Forchheimer equation (Whitaker 1996; Konzuk and Kueper 2004; Qian et al. 2011; Kong et al. 2018). Su (1997) and Hu et al. (2005) studied the local flow state in cross fractures. According to the fluid momentum equation and considering the velocity head, the local head loss equation of a cross fracture with an undetermined coefficient was derived. Johnson et al. (2006) observed the morphology of dyed fluid flow through rough cross-fracture model tests and concluded that rough cross fractures greatly increase the mixing of fluid at fracture intersections. Zhu et al. (2013) pointed out that due to the intersection and deflection of fluids in cross fractures, the actual pressure drop at both ends of the fracture, which was larger than the theoretical pressure drop, was defined as the excess pressure drop loss, and the excess pressure drop loss coefficient $\zeta$ was proposed to quantify the degree of pressure loss.

At present, discrete fracture networks (DFNs) are widely applied in the study of fracture network seepage and attain a good application effect in solving large-scale engineering problems, but research on fracture network seepage is relatively limited at the mesoscale (Kulatilake and Panda, 2000; Chen et al. 2008; Klimczak et al. 2010; Wu and Kulatilake 2012; Zhang et al. 2012). Through the study of the flow distribution in a fracture network, it has been found that fluid flow mainly occurs in long fractures parallel to the direction of fluid flow or hydraulic gradient, especially in those fractures intersecting with the entrance and exit boundaries of the model, thus forming the dominant flow path in fracture network seepage (Liu et al. 2015; Yu et al. 2017). Research on the seepage characteristics of fracture networks with regular geometries, represented by basalt columnar jointed rock masses, has become a new research topic of heightened interest. Researchers have mainly studied this topic through the physical model test method. The corresponding theoretical model has seldom considered the nonlinear seepage characteristics of cross fractures, so it does not suitably quantify the loss value (Zou et al. 2013; Niu et al. 2020). Based on the research of the above scholars, at present, scholars do not fully understand the phenomenon of energy loss caused by head loss, have not formed a theoretical model that can describe the head loss in complex fracture network, and lack of understanding of the meso mechanism of head loss effect.

To further study the influence of the local head loss on the seepage characteristics of the fracture network, the fracture network has been simulated as an electric circuit network (Kong et al. 2018). Considering the local pressure drop loss effect at the intersection of fractures, an equivalent local loss resistance model is established based on the equivalent seepage resistance model. Moreover, aiming at the common cross-section forms of columnar joints, physical models of quadrilateral and hexagonal fracture networks are established, and seepage tests under different pressure drop conditions are carried out based on these physical models. Finally, the test results are compared to theoretical calculation results. With the use of general-purpose CFD software FLUENT, the microscale flow state in the fracture network is analyzed, and streamline and velocity vector characteristics of the fracture network are obtained. Hence, a comprehensive analysis of the seepage characteristics of a complex fracture network considering local loss is realized.

## Methodology

The research method is divided into three parts, and the technical roadmap of this study is shown in Fig. 1.

### Equivalent circuit characteristics of the fracture network

The fracture network is composed of a limited number of single fractures, and the most basic connection modes are the two modes shown in Fig. 2. The seepage law of smooth single fracture conforms to the cubic law, in which the volumetric flow $q$ through the fracture can be expressed as:

$$q = \frac{\rho g w e^3}{12\mu} J \tag{1}$$

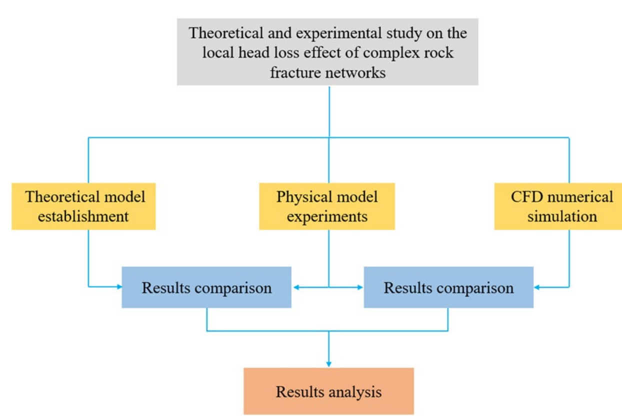


**Fig. 1** The technology roadmap of the work

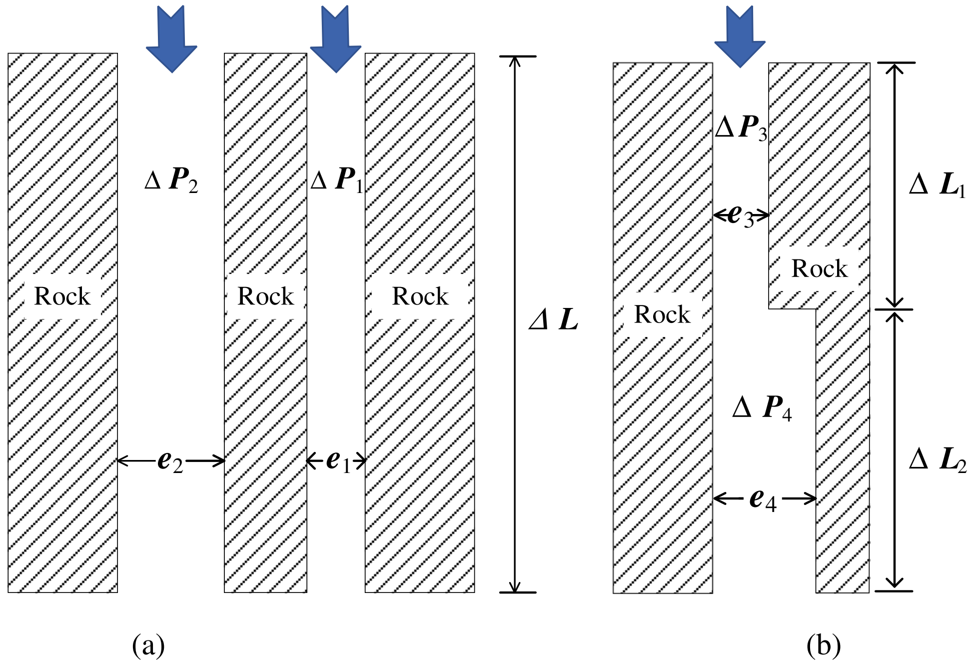


**Fig. 2** Different connection modes of fractures: **a** parallel connection mode of fractures, **b** series connection mode of fractures

where $\rho$ is the density of the fluid, $g$ is the acceleration of gravity, $w$ is the thickness of the fracture, $e$ is the opening of the fracture, $\mu$ is the dynamic viscosity coefficient of the fluid, and $J$ is the hydraulic gradient along the flow direction.

The parallel connection mode of fractures can be simplified, as shown in Fig. 2a, and the total fracture flow is equal to the sum of the flow through the two connected fractures:

$$q_J = q_1 + q_2 = \frac{we_1^3}{12\mu C_1}\frac{\Delta P_1}{\Delta L} + \frac{we_2^3}{12\mu C_2}\frac{\Delta P_2}{\Delta L} \quad (2)$$

where $q_J$ is the total fracture flow, $q_1$ and $q_2$ are the flow amounts through the two fractures, $\Delta P_1$ and $\Delta P_2$ are the pressure drops in the two fractures, $C_1$ and $C_2$ are the roughness correction coefficients of the two fractures, $\Delta L$ is the lengths of the fractures, $e_1$ and $e_2$ are the widths of the two fractures, and $w$ is the thickness of the fracture.

Correspondingly, the series connection mode of fractures is shown in Fig. 2b, and the total pressure drop of the connected fractures is equal to the sum of the pressure drop of each fracture:

$$\Delta P = \Delta P_3 + \Delta P_4 = \frac{12\mu C_3 \Delta L_1}{we_3^3} q_3 + \frac{12\mu C_4 \Delta L_2}{we_4^3} q_4 \quad (3)$$

Comparing Eqs. (2) and (3), it is observed that a common $12\mu C\Delta L/we^3$ term occurs in both equations. Tao and Liu (2012) defined this term as the equivalent seepage resistance $R_f$, so the seepage characteristics of a given fracture network are equivalent to the current characteristics of a circuit. Zhu et al. (2013) found that the calculated value of the total pressure drop attributed to an abrupt change in the fracture width within a fracture network is smaller than the test value and defined the loss difference as the excess water pressure drop loss. This phenomenon is caused by the following two factors: one factor is the change in velocity due to the abrupt change in fracture width, and the other factor is the change in the fluid flow state due to the abrupt change in fracture width. The loss coefficient of the excess water pressure drop $\zeta$ is defined as:

$$\zeta = \frac{\Delta P_c}{\Delta P} \le 1 \quad (4)$$

where $\Delta P$ is the measured water pressure drop and $\Delta P_c$ is the calculated water pressure drop. The dimensionless expression of the water pressure drop $\Delta P$ is $\Delta p$. Substituting this dimensionless expression in Eq. (3), the following is obtained:

$$\zeta = \frac{24e_3^2 L}{\Delta p \mathrm{Re}}\left(\frac{1}{e_3^3} + \frac{1}{e_4^3}\right) \quad (5)$$

$$\mathrm{Re} = \rho v L/\mu \quad (6)$$

where $\rho$ is the fluid density and $\mu$ is the dynamic viscosity coefficient, Re is the Reynolds number and $v$ is the characteristic velocity of the flow field.

There are two types of fracture connections: gap width contraction and gap width expansion. Along the flow direction, the excess water pressure drop under the condition of gap width expansion can be ignored, and the relationship between $\Delta p$ and Re is as follows (Zhu et al. 2013):

$$\Delta p = 0.6 + 14.14/[\mathrm{Re}(e_1/2L)], \mathrm{Re} \le \mathrm{Rec}) \tag{7}$$

where Rec is the critical Reynolds number. In addition, the dip angle is also an inherent property of fractures, and experimental research has shown that in most cases, the loss attributed to the excess water pressure drop caused by the fracture dip angle can be expressed based on the increase in fracture flow distance.

## Establishment of the E-loss model of the fracture network

The most basic form of the mixed connection mode of a single-inlet fracture network is the single-inlet series parallel hybrid connection mode, as shown in Fig. 3.

Under this connection mode, without considering the loss attributed to the excess water pressure drop at the contraction position of the gap width, the total flow $q_J$ of the fracture is as follows:

$$q_J = \Delta P/R_J = \Delta P/(\frac{12\mu C_2 C_3 L}{we_3^3 C_2 + we_2^3 C_3} + \frac{12\mu C_1 L}{we_1^3}) \tag{8}$$

where $R_J$ is the total seepage resistance of the fracture.

It is difficult to consider the head loss based on the loss coefficient of the excess water pressure drop. Therefore, in previous research work, scholars have applied a simplified method to consider only the water pressure loss along the dominant seepage path. At $e_2 << e_3$, the simplified method is more reasonable, but when $e_2$ approaches $e_3$, the simplified method is not applicable (Sang et al. 2016).

To consider the head loss in the fracture network under the different fracture modes more accurately, the loss is defined as the equivalent local loss resistance $R_x$. As shown in Fig. 2b, the equivalent local loss resistance $R_x$ can be expressed as:

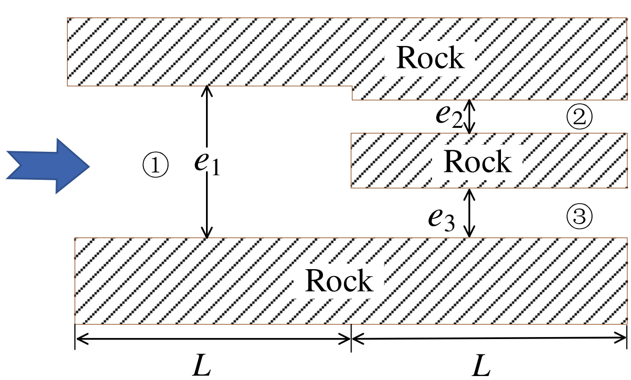


**Fig. 3** Single-inlet series parallel hybrid connection mode

$$R_x = R_J - (R_{f3} + R_{f4}) = \frac{\Delta P}{q} - \frac{\Delta P_c}{q} = \frac{1-\zeta}{\zeta}(R_{f3} + R_{f4}) \tag{9}$$

where $R_{f3}$ and $R_{f4}$ denote the seepage resistance values of the two fractures connected in series. Substituting Eq. (9) into Eq. (7), $R_x$ can be expressed as:

$$R_x = (\frac{0.6\mathrm{Re}(e_3/L) + 28.28}{24[1 + (e_3/e_4)^3]} - 1)(R_{f3} + R_{f4}) \tag{10}$$

Based on the above equation, the key to model application to mixed joint fractures, as shown in Fig. 3, is to determine the Reynolds number of each fracture. To facilitate analysis, the ratio of the Reynolds number of the branch fractures (fractures ② and ③) to that of the main fractures (fracture ①) is defined as the Reynolds number distribution coefficient $\alpha$:

$$\alpha_i = \frac{\mathrm{Re}_i}{\mathrm{Re}} \tag{11}$$

Combining Eqs. (9), (10), and (11), the equivalent local loss resistance $R_{x2}$ of the fracture branch ② and the equivalent local loss resistance $R_{x3}$ of the fracture branch ③ can be obtained as follows:

$$R_{x2} = (\frac{0.6e_2\mathrm{Re}/L[(e_3/e_2)^3 + 1] + 28.28}{24[1 + (e_2/e_1)^3]} - 1)(R_{f1} + R_{f2}) \tag{12}$$

$$R_{x3} = (\frac{0.6e_3\mathrm{Re}/L[(e_2/e_3)^3 + 1] + 28.28}{24[1 + (e_3/e_1)^3]} - 1)(R_{f1} + R_{f3}) \tag{13}$$

The total flow through the fracture network and the flow through each branch can be expressed as follows:

$$q_J = \Delta P/R_J = \Delta P/(R_{f1} + \frac{(R_{x2} + R_{f2})(R_{x3} + R_{f3})}{R_{x2} + R_{f2} + R_{x3} + R_{f3}}) \tag{14}$$

$$q_2 = q_J \cdot \alpha_2, q_3 = q_J \cdot \alpha_3 \tag{15}$$

The most basic form of the mixed-connection mode of a fracture network with dual inlets is the cross-shaped fracture formed by the intersection of two fractures, as shown in Fig. 4.

Tian (1986) divided the water flow in a cross fracture into three streams through dye tracer tests: the $\alpha$ stream from the narrow fracture passing through the intersection to the wide fracture; the $\beta$ stream from the wide fracture passing through the intersection to the narrow fracture, and the third stream from the wide fracture passing through the intersection to the wide fracture. Among these three flows, only the $\beta$ flow passes through the contraction joint, so only the equivalent local loss resistance caused by the $\beta$

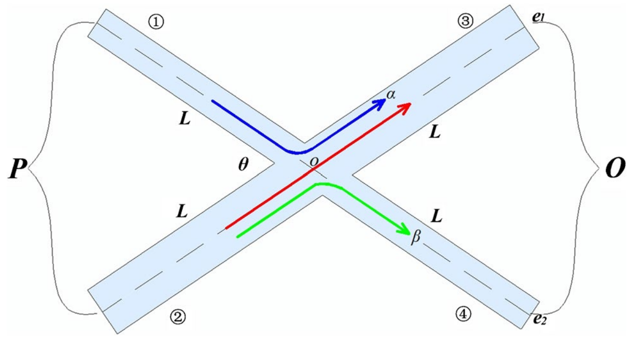


**Fig. 4** Dual-inlet series parallel hybrid connection mode

flow should be considered. According to the E-loss model, the total discharge of cross fractures is as follows:

$$q_J = P/(R'_f + R''_f) = \frac{(R_{f1} + R_{f2})(R_{f1} + R_{f2} + R_x)}{2R_{f1} \cdot R_{f2}(R_{f1} + R_{f2} + R_x) + R_{f2}^2 \cdot R_x} P \quad (16)$$

In the above equation, $R'_f$ and $R''_f$ are the equivalent seepage resistance values of the left and right sides, respectively, of the o point, and $R_x$ is the equivalent local loss resistance caused by the $\beta$ flow.

Through the above analysis, with the E-loss model, the seepage problem of a complex parallel connection fracture network can be decomposed into an equivalent circuit problem including multiple equivalent seepage resistance and equivalent local loss resistance values, and the flow distribution in each fracture of the fracture network can be obtained by an iterative method. The physical meaning is clear, and the calculation accuracy is high.

## Scheme and method of the physical model test

Combined with the research on the seepage characteristics of fracture networks in columnar jointed rock masses, physical models of quadrilateral fracture networks and hexagonal fracture networks are established to study the local head loss effect in complex fracture networks. In this paper, quadrilateral and hexagonal fracture networks are designed and manufactured with smooth plexiglass as the main material, as shown in Fig. 5. The whole test device consists of three parts: a fixed water head device (responsible for providing a controllable and stable fixed water head), a fracture network model (the main test area), and a

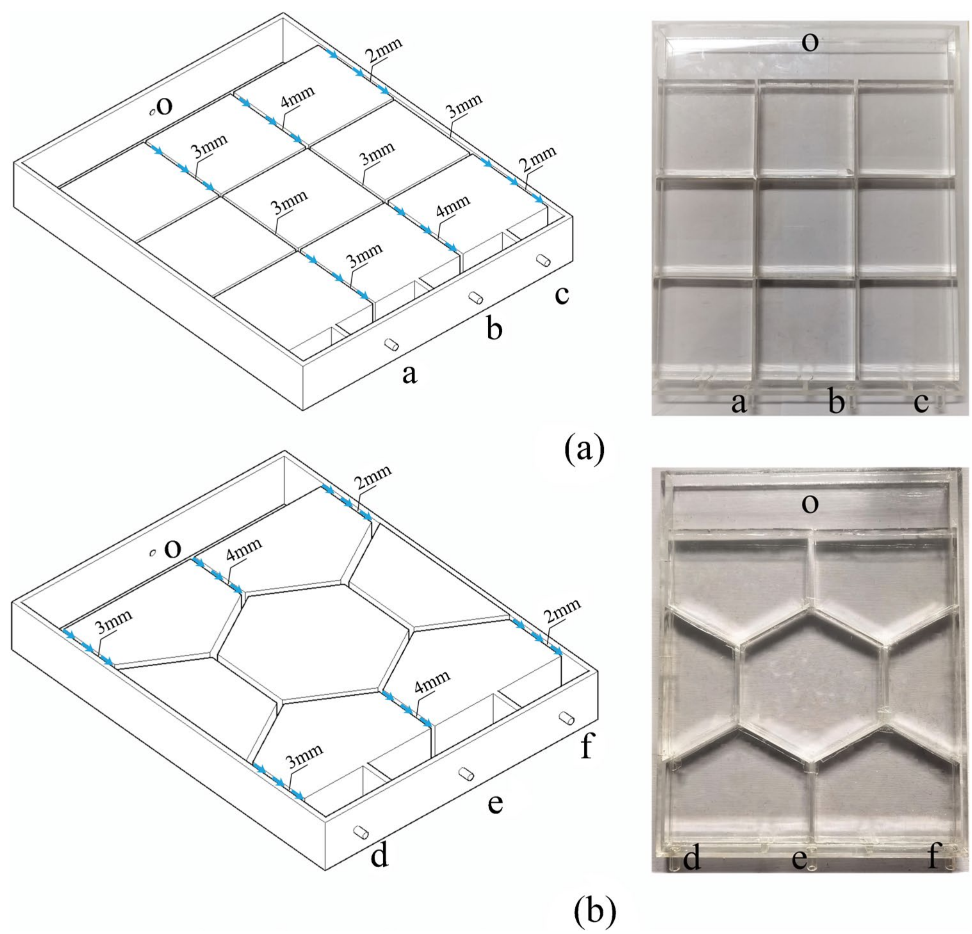


**Fig. 5** Fracture network model: **a** quadrilateral fracture network model, **b** hexagonal fracture network model

pressure measuring device (responsible for measuring the water head at each outlet of the fracture network).

The physical model test is divided into four steps:

: Connect the reserved holes of the fracture network model to the corresponding positions with rubber pipes and assess the sealing effect of the whole model.

: Lift the constant-head water tank to a suitable height, rotate the ball valve to adjust the water head, ensure that there are no bubbles in the model, and record the water head at the inlet and outlet ends after the flow rate has stabilized.

: Measure the outflow amount at the three outlets and determine the average value of three measurements for each group.

: Gradually raise the constant-head device through the automatic lifting device and repeat the second and third steps to obtain the flow distribution at each outlet of the fracture network under different pressure drops.

## Establishment of the numerical model

Computational fluid dynamics (CFD) has been widely applied to calculate the flow around single or multiple pipes within a large Reynolds number range (Lam et al. 2008). CFD software FLUENT based on the finite volume method is used to solve the corresponding Navier Stokes equations. The mass conservation equation or continuity equation in the fluid domain without a confluence source is as follows (Zhang et al. 2021):

$$\frac{\partial\rho}{\partial t}+\nabla(\rho\vec{v})=0 \tag{17}$$

where $\rho$ is the density of the liquid, $t$ is the time, and $\vec{v}$ is the velocity vector.

The law of momentum conservation represents the change in force in the fluid domain, and the momentum equation is expressed as follows:

$$\frac{\partial}{\partial t}(\rho\vec{v})+\nabla\cdot(\rho\vec{v}\vec{v})=-\nabla p+\nabla\cdot(\overline{\overline{\tau}})+\rho\vec{g}+\vec{F} \tag{18}$$

where $p$ is the static pressure, $\overline{\overline{\tau}}$ is the stress tensor, and $\rho\vec{g}$ and $\vec{F}$ are the gravitational body force and external body force, respectively.

In this paper, a three-dimensional model is established according to the actual model size. Three-dimensional modeling diagrams of the fluid domain of the above two fracture networks are shown in Fig. 6. The model is subsequently meshed. Due to the complexity of the model, an unstructured mesh is adopted, which mainly comprises tetrahedra, thus accelerating the convergence process of the solver. The two fracture network models are composed of 450,000 and 400,000 elements. After modeling, they are imported into the Fluent solver for calculation.

The k-ε model is chosen as the turbulence model in the solver. The k-ε model was first put forward in the 1970s. It is a semiempirical equation established by W.P. Jones and B.K. Lauder considering experimental phenomena. The k-ε model is a two-equation turbulence model. The advantage of this model is that it improves the mixing length model and avoids the algebraic expression of the turbulent length in complex flow, so it achieves a good calculation effect and good stability and economy. In the pressure velocity coupling method, the pressure implicit with splitting of operators (PISO) algorithm, which yields obvious advantages in solving transient problems, is adopted. The method performs two additional corrections, namely, adjacency correction and skew correction, which makes the calculation process more efficient. The gradient term is based on the least-square method of the elemental volume, and the pressure interpolation scheme is based on the volume force weighting scheme. The wall adopts the assumption of fixed nonslip boundary. In terms of water head, it is set as a fixed pressure head according to the test conditions, and the outlet boundary is set as atmospheric pressure boundary.

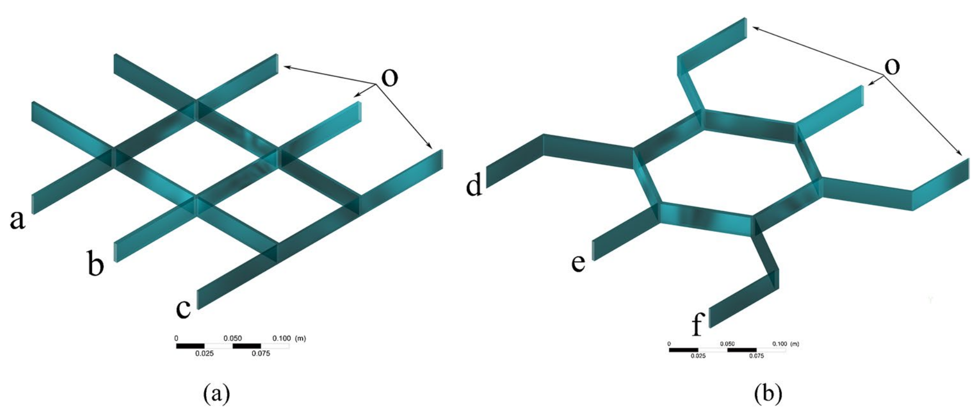


**Fig. 6** Three-dimensional models: **a** quadrilateral fracture network model, **b** hexagonal fracture network model

## Results and discussion

### Experimental results and analysis of the quadrilateral fracture network

The outlet flow ($q_a$, $q_b$, and $q_c$) at the three outlets (a, b, and c, respectively) of the quadrilateral fracture network under different pressure drop conditions and the total discharge $q_J$ are listed in Table 1.

Based on the experimental phenomena, it is observed that with increasing water pressure, the Reynolds number of the flow through each fracture gradually increases, and the main flow form in the fracture network changes from laminar flow to turbulent flow. Under a low pressure, the flow in the system mainly occurs in the stable laminar state, and the flow rate and total flow rate at each outlet are approximately linear with the water pressure drop. With increasing water pressure, the flow rate and water pressure drop attain a nonlinear corresponding relationship. In addition, due to the different water carrying capacities of each fracture in the fracture network system, the corresponding water pressure drop associated with each fracture flow regime is different, and the flow regime at each outlet changes to turbulent flow with decreasing gap width.

With increasing water pressure, the proportion of flow at outlet a slightly increases, the proportion of flow at outlet b notably decreases, and the proportion of flow at outlet c increases significantly. The evolution of the flow rate can be divided into the following three stages: ① at the laminar flow stage of the fracture network, when the pressure drop is small (smaller than 250 Pa), all single fractures occur in the laminar flow state, the seepage characteristics of the fracture network are only affected by the head loss at each node, and the flow rate at each fracture outlet remains almost constant. ② At the turbulent development stage of the fracture network, with increasing water pressure drop, the flow state in the fracture network part with a larger gap width first develops to turbulent flow, and the resistance of the fluid further increases. However, the flow state in the fractures with smaller gap widths is laminar flow, which leads to a decrease in the proportion of flow in the fractures with larger gap widths. The corresponding test results indicate that the proportion of fracture flow at outlet c greatly increases. ③ In the turbulent phase of the fracture network, when the water pressure drop is large enough (larger than 613 Pa), the main flow through the fractures of the fracture network enters the turbulent state. Subsequently, the fluid in each fracture is affected by turbulence, and the resistance increases. The further diversion effect caused by the turbulence in the large-width fractures weakens, and the proportion of flow at each outlet fracture tends to remain stable.

The numbered quadrilateral fracture network model is shown in Fig. 7a, and the results of the dyed tracer test are shown in Fig. 7b. The calculation results of the water flow through each fracture with the E-loss model proposed above are listed in Table 2.

The tracer test reveals the water flow direction in the fracture network, and it is observed that the fluid in fracture 2 flows into fractures 7 and 9 through fractures 5 and 6. The fluid in fractures 7 and 9 then flows into fracture 14 through fractures 11 and 12, respectively. Moreover, the water velocity in transverse fractures 5, 6, and 11 is lower than that in longitudinal fractures 1, 2, 7, and 8. Table 2 provides the flow rate in each fracture calculated with the E-loss model. Based on the calculation results, it is found that the model reflects the results of the tracer test and verifies the rationality of the basic assumptions of the model.

Furthermore, the experimental results of the total discharge of the quadrilateral fracture network under the different pressure drop conditions, the calculation results of the local cubic law and the calculation results of the E-loss model are comprehensively shown in Fig. 8.

**Table 1** Test results of the outlet flow of the quadrilateral fracture network

| ΔP/Pa | $q_a$/mL·s$^{-1}$ | $a$/% | $q_b$/mL·s$^{-1}$ | $b$/% | $q_c$/mL·s$^{-1}$ | $c$/% | $q_J$/mL·s$^{-1}$ |
|---|---|---|---|---|---|---|---|
| 50 | 4.75 | 28.3 | 10.15 | 60.4 | 1.9 | 11.3 | 16.8 |
| 102 | 9.51 | 29.1 | 19.23 | 58.9 | 3.92 | 12.0 | 32.66 |
| 157 | 13.75 | 29.2 | 27.45 | 58.4 | 5.84 | 12.4 | 47.04 |
| 250 | 21.13 | 29.9 | 39.56 | 56.1 | 9.87 | 14.0 | 70.56 |
| 335 | 26.01 | 29.7 | 44.26 | 50.6 | 17.23 | 19.7 | 87.5 |
| 478 | 38.56 | 32.2 | 58.47 | 48.8 | 22.75 | 19.0 | 119.78 |
| 613 | 43.54 | 32.1 | 62.71 | 46.3 | 29.23 | 21.6 | 135.48 |
| 793 | 47.45 | 31.8 | 66.79 | 44.8 | 34.78 | 23.4 | 149.02 |
| 1186 | 54.26 | 32.8 | 74.15 | 44.8 | 37.11 | 22.4 | 165.52 |
| 1499 | 62.03 | 32.9 | 84.30 | 44.7 | 42.41 | 22.4 | 188.74 |
| 1744 | 66.79 | 32.8 | 90.56 | 44.5 | 46.02 | 22.7 | 203.37 |
| 1960 | 68.90 | 32.9 | 92.95 | 44.4 | 47.67 | 22.7 | 209.52 |

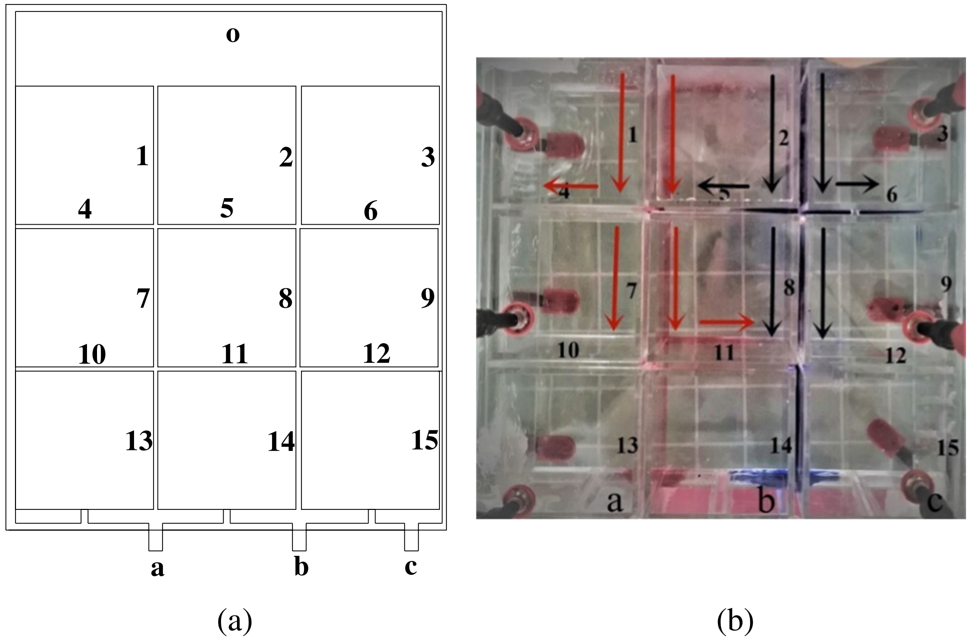


**Fig. 7** Experimental results of the quadrilateral fracture network: **a** fracture network number, **b** results of the dyed tracer test

**Table 2** Flow calculation of the quadrilateral fracture network

| ΔP/Pa | Flow value $q$/mL·s$^{-1}$ | | | | | | | | | | | | |
|---|---|---|---|---|---|---|---|---|---|---|---|---|---|
| | 1 | 2 | 3 | 5 | 6 | 7 | 8 | 9 | 11 | 12 | 13 | 14 | 15 |
| 50 | 5.05 | 10.3 | 1.95 | 0.72 | 2.23 | 5.77 | 7.33 | 4.18 | 0.72 | 2.23 | 5.05 | 10.3 | 1.95 |
| 102 | 10.2 | 19.7 | 4 | 1.85 | 4.99 | 12 | 12.9 | 8.99 | 1.82 | 5.13 | 10.2 | 19.8 | 3.86 |
| 157 | 15 | 28 | 6.11 | 3.17 | 7.41 | 18.2 | 17.4 | 13.5 | 3.05 | 8.15 | 15 | 28.6 | 5.37 |
| 250 | 23.3 | 41 | 9.88 | 5.59 | 11.4 | 28.9 | 24 | 21.2 | 5.37 | 13.7 | 23.3 | 43.1 | 7.5 |
| 335 | 31 | 51.5 | 13.4 | 7.69 | 14.7 | 38.7 | 29.2 | 28.1 | 7.58 | 19.1 | 31 | 55.8 | 9.03 |
| 478 | 44 | 67.6 | 19.5 | 11 | 19.6 | 55 | 37 | 39.1 | 11.4 | 28.2 | 44 | 76.5 | 11 |
| 613 | 56.4 | 81.4 | 25.4 | 13.9 | 23.8 | 70.4 | 43.7 | 49.2 | 15 | 36.9 | 56.4 | 95.6 | 12.3 |
| 793 | 73 | 97.7 | 33.4 | 17.7 | 29 | 90.7 | 51.1 | 62.4 | 20.1 | 48.8 | 73 | 120 | 13.6 |
| 1186 | 109 | 127 | 51.1 | 26 | 39.8 | 135 | 61.4 | 90.8 | 31.8 | 75.6 | 109 | 169 | 15.3 |
| 1499 | 139 | 151 | 65.7 | 30 | 46.3 | 169 | 74.9 | 112 | 41.3 | 95.9 | 139 | 212 | 16.1 |
| 1744 | 162 | 165 | 77.8 | 34.3 | 52.1 | 197 | 78.8 | 130 | 47.7 | 114 | 162 | 240 | 16.2 |
| 1960 | 184 | 180 | 87.8 | 36.9 | 55.2 | 221 | 87.6 | 143 | 53.8 | 126 | 184 | 268 | 16.7 |

Figure 8 shows that when the water pressure drop $\Delta p$ is small, the outlet flow calculated with the local cubic law is larger than the test value because the excessive water pressure drop loss at the fracture intersections is not considered, and the flow calculated with the method proposed in this paper is closer to the test data, thus verifying the applicability of the E-loss model. With increasing fracture water pressure drop, turbulent flow occurs in some fractures of the fracture network, but the basic assumption of the E-loss model is that fracture flow conforms to linear Darcy flow. Therefore, the calculation results based on this model gradually deviate from the test data, but they are still closer to the test values than those obtained with the cubic law, which achieves a certain correction effect. The process can be observed more intuitively with the total fracture discharge diagram. When the water pressure drop is larger than 613 Pa, the nonlinear characteristics of the overall fracture discharge rapidly increase. The boundary is defined as the laminar turbulent boundary (L–T line). When the pressure drop $\Delta p$ is located below the L–T line, the experimental and theoretical values exhibit a higher fitting value. When the Reynolds number in each fracture of the fracture network continues to rise, the resultant turbulent flow exhibits nonlinear characteristics, and the calculated values of the seepage model based on the local cubic law deviate, so the turbulent flow theory should be considered to describe the deep flow characteristics of the fracture network, i.e., the characteristics above the L–T line.

By observing the relationship between the flow rate and the water pressure drop at each outlet, it is found that when

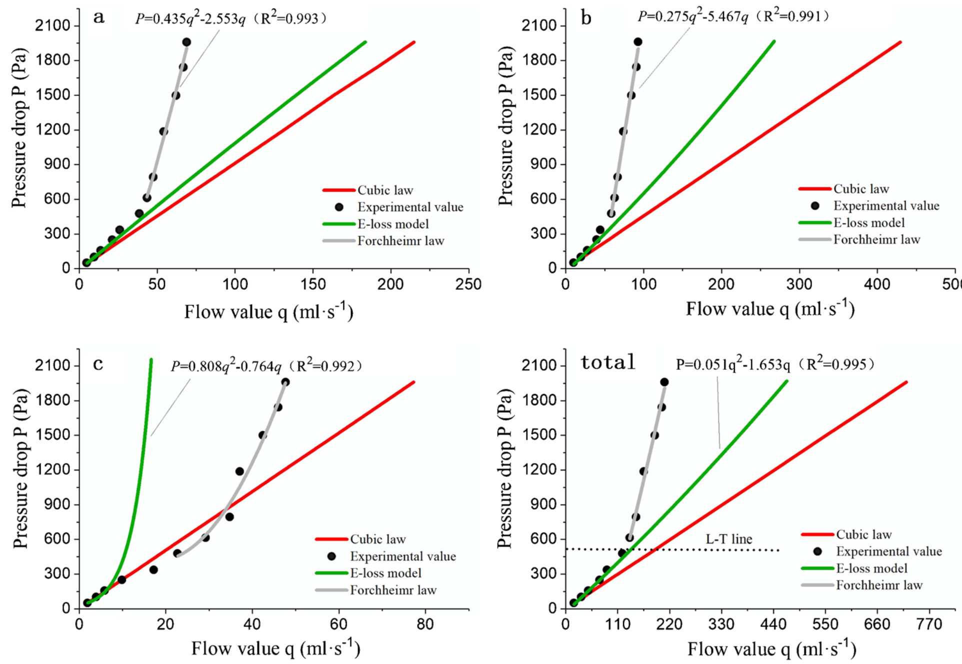


**Fig. 8** Comparison diagram of the test results and theoretical calculation results

the water pressure drop exceeds 250 Pa and less than 600 Pa, the actual flow rate at outlets a and b is lower than the theoretical calculation results based on the E-loss model, However, the flow value at outlet c even exceeding the calculation value obtained with the local cubic law, which is further verified: when the water pressure drop is larger than 250 Pa and some turbulent fracture fluid flow occurs, the resistance of the fluid in the turbulent region increases, and the fluid in the large-gap width fractures is further distributed into the small-gap width fractures. Therefore, the flow at outlet c increases, and the flow rate is higher than the calculated value obtained with the cubic law. However, with increasing pressure drop, when the water pressure drop is larger than 600 Pa, the fluid flow in the small-gap width fractures gradually transitions into turbulent flow, and the influence of turbulence effect in large-gap width fractures on the flow of small-gap width fractures is reduced, which results in a lower flow rate at outlet c than that calculated with the cubic law but still higher than that calculated with the E-loss model.

Above the L–T line, with increasing water pressure drop, the flow in each fracture of the fracture network gradually transitions to the turbulent flow state. With the use of the research method of Qian (Qian et al. 2011), the Forchheimer equation is adopted to fit the outlet flow and total flow. The fitting results reveal that the determination coefficient $R^2$ of the discharge at each outlet and the total discharge is higher than 0.99, which suggests that the seepage characteristics of the fracture network can be described with the Forchheimer equation under turbulent flow conditions.

## Experimental results and analysis of the hexagonal fracture network

The same analysis method is used to analyze the experimental results of the hexagonal fracture network, and the outlet flow ($q_d$, $q_e$, and $q_f$) at the three outlets (d, e, and f, respectively) of the hexagonal fracture network under the different pressure drop conditions and the total discharge $q_J$ are listed in Table 3.

The numbered hexagonal fracture network model is shown in Fig. 9a, and the results of the dyed tracer test are shown in Fig. 9b. The calculation results of fracture water flow by using the E-loss model proposed above are provided in Table 4.

According to the test data in Table 4, the flow evolution in the hexagonal fracture network is similar to that in the quadrilateral fracture network: the flow rate at each outlet is different, and the flow rate in the fractures with a larger gap width is higher. With increasing water pressure drop, the flow rate at the three outlets changes, the flow rate at outlet d slightly fluctuates, the flow rate at outlet d fluctuates slightly, the flow rate at outlet e decreases notably, and the flow rate at outlet f significantly increases. This also demonstrates that there are three stages in the hexagonal fracture network: the laminar flow stage, turbulent flow development stage and turbulent flow stage. In addition, the tracer test reveals that the dominant flow effect is obvious in the hexagonal fracture network.

The experimental results of the flow rate of the hexagonal fracture network under the different pressure drop conditions, the calculation results of the local cubic law and the

**Table 3** Test results of outlet flow of hexagonal fracture network

| ΔP/Pa | $q_d$/mL·s$^{-1}$ | $d$/% | $q_e$/mL·s$^{-1}$ | $e$/% | $q_f$/mL·s$^{-1}$ | $f$/% | $q_J$/mL·s$^{-1}$ |
|---|---|---|---|---|---|---|---|
| 100 | 8.01 | 27.5 | 17.78 | 61.0 | 3.35 | 11.5 | 29.14 |
| 150 | 11.12 | 27.2 | 24.67 | 60.5 | 5.02 | 12.3 | 40.81 |
| 198 | 15.21 | 28.7 | 31.11 | 58.7 | 6.68 | 12.6 | 53.00 |
| 245 | 18.89 | 29.0 | 37.98 | 58.3 | 8.31 | 12.7 | 65.18 |
| 392 | 26.58 | 31.1 | 45.89 | 53.6 | 13.10 | 15.3 | 85.57 |
| 498 | 31.71 | 32.5 | 49.86 | 51.2 | 15.86 | 16.3 | 97.43 |
| 615 | 36.32 | 34.1 | 52.21 | 49.1 | 17.89 | 16.8 | 106.42 |
| 891 | 40.15 | 34.7 | 54.33 | 47.0 | 21.12 | 18.3 | 115.60 |
| 1215 | 45.23 | 35.3 | 56.21 | 43.8 | 26.81 | 20.9 | 128.25 |
| 1607 | 48.89 | 35.0 | 57.67 | 41.3 | 33.06 | 23.7 | 139.62 |
| 1813 | 50.50 | 34.8 | 58.89 | 40.6 | 35.62 | 24.6 | 145.01 |
| 2018 | 51.22 | 34.3 | 61.34 | 41.1 | 36.70 | 24.6 | 149.26 |

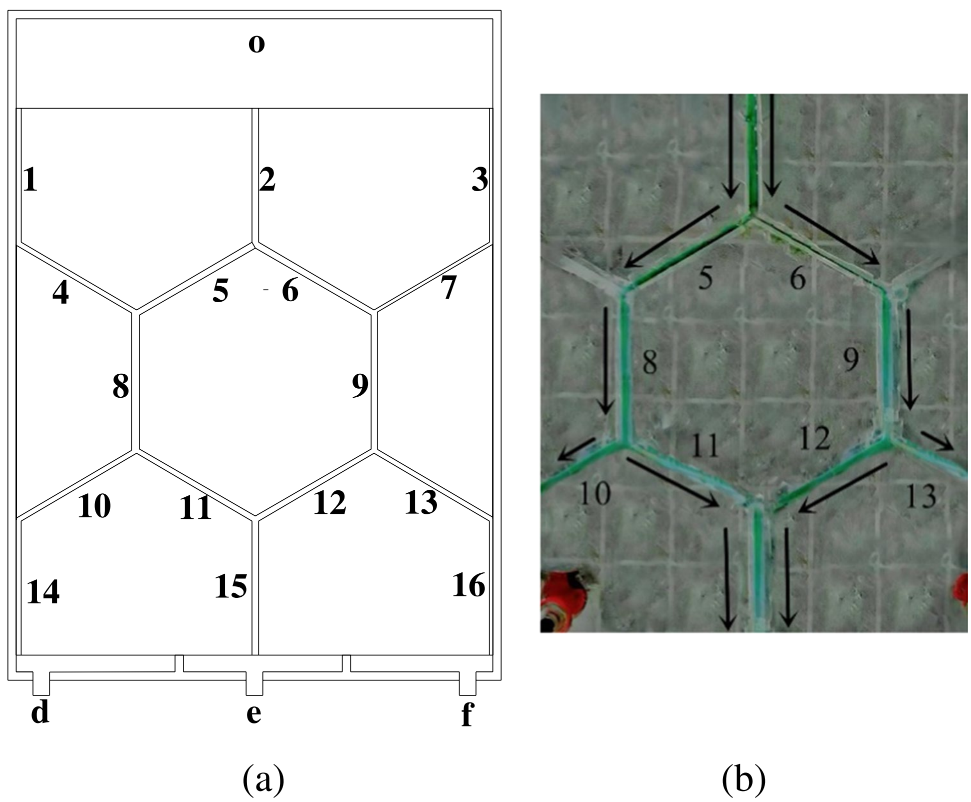


**Fig. 9** Experimental results of the hexagonal fracture network: **a** fracture network number, **b** results of the dyed tracer test

calculation results of the E-loss model are comprehensively shown in Fig. 10.

Figure 10 shows that the E-loss model basically reflects the water flow evolution in the fracture network under laminar flow conditions (below the L–T line). The flow rate at each outlet and the total flow rate under turbulent flow condition can be fitted with the Forchheimer equation, and the coefficient of determination $R^2$ of the fitting results is higher than 0.99. Combined with the fitting results of the quadrilateral fracture network, the quadratic fitting equation suitably describes the seepage characteristics of the fracture network at the turbulent stage.

## Analysis of the numerical simulation results

The vector graph directly shows the direction and size of a given vector (such as the velocity) in two-dimensional or three-dimensional space. The velocity vector diagram is an effective means to reflect the velocity change, vortices, reflux conditions, etc. It is one of the most commonly adopted maps in flow field analysis. By default, the vector

**Table 4** Flow calculation results of the hexagonal fracture network

| ΔP/Pa | Flow value $q$/mL·s$^{-1}$ | | | | | | | | | | | |
|---|---|---|---|---|---|---|---|---|---|---|---|---|
| | 1 | 2 | 3 | 5 | 6 | 8 | 9 | 11 | 12 | 14 | 15 | 16 |
| 100 | 8.38 | 22 | 2.64 | 10.6 | 11.4 | 19 | 14 | 10.4 | 9.92 | 8.52 | 20.4 | 4.11 |
| 150 | 12.4 | 29.6 | 4.02 | 14 | 15.6 | 26.4 | 19.6 | 14.4 | 13.5 | 12 | 27.9 | 6.12 |
| 198 | 16.1 | 35.9 | 5.37 | 16.9 | 19 | 33 | 24.4 | 18 | 16.4 | 15 | 34.4 | 7.94 |
| 245 | 19.6 | 41.4 | 6.69 | 19.3 | 22.1 | 38.8 | 28.8 | 21.1 | 19.2 | 17.8 | 40.2 | 9.65 |
| 392 | 29.8 | 55.7 | 10.8 | 25.2 | 30.6 | 55 | 41.4 | 29.2 | 26.7 | 25.8 | 56 | 14.6 |
| 498 | 36.7 | 64.6 | 13.8 | 29.4 | 35.3 | 66 | 49.1 | 35.7 | 31 | 30.4 | 66.7 | 18.1 |
| 615 | 43.9 | 73.3 | 17.1 | 32.8 | 40.5 | 76.6 | 57.6 | 41.1 | 36 | 35.6 | 77.1 | 21.6 |
| 891 | 59.5 | 90.3 | 24.6 | 39.8 | 50.5 | 99.2 | 75.1 | 53.1 | 45.9 | 46.2 | 99 | 29.2 |
| 1215 | 76.1 | 104 | 33.2 | 45 | 59.4 | 121 | 92.6 | 64.4 | 54.9 | 56.8 | 119 | 37.7 |
| 1607 | 94.4 | 122 | 43.3 | 51.6 | 70.2 | 146 | 113 | 77.5 | 67 | 68.4 | 145 | 46.4 |
| 1813 | 103 | 129 | 48.5 | 52.8 | 76.5 | 156 | 125 | 81.9 | 74.6 | 74.3 | 157 | 50.4 |
| 2018 | 112 | 136 | 53.5 | 58.8 | 76.9 | 170 | 130 | 91.2 | 75 | 79.3 | 166 | 55.3 |

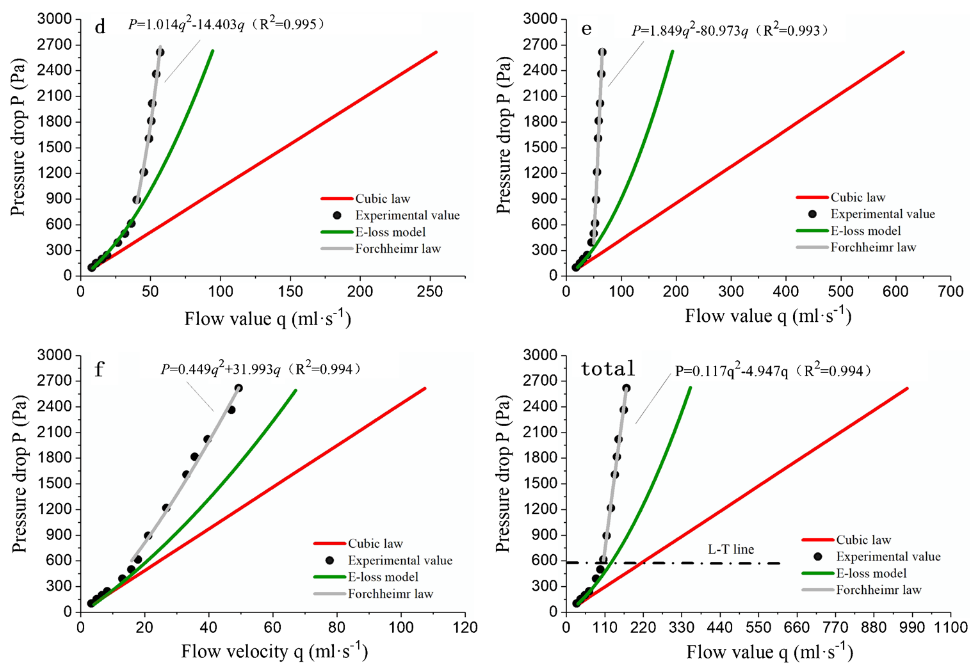


**Fig. 10** Comparison diagram of the test results and theoretical calculation results

is drawn at the center of each grid cell, the direction of the vector is indicated with an arrow, and the size of the vector is indicated by the length and color of the arrow. Different colored lines are applied to represent the trajectory of particles and visualize the flow of massless particles in the computational domain. The user may specify the surface from which the particles are released. By describing the streamline diagram and velocity vector diagram of the two models under turbulent conditions, the motion state of the fluid and the distribution of the velocity field in the fluid domain in response to a sudden change in the gap width can be clearly defined. Velocity vector distribution diagrams of the quadrilateral and hexagonal models under the condition of 150 Pa are shown in Figs. 11 and 12, respectively. In both models, three fracture junctions (gap width mutation) are selected, the symmetrical cross sections along the thickness direction are cut to obtain the mesoscale streamline diagram in the plane, and the streamline diagram is displayed on both sides of the vector diagram.

In the velocity vector diagram and streamline diagram of the fracture network, the flow direction and velocity distribution of water flow in the two fracture networks are clearly reflected under the same pressure inlet gradient. Under the action of a pressure entrance, an entrance with a larger fracture aperture obtains a higher initial velocity. Choosing the quadrilateral fracture network as an example, the flow velocity at the middle entrance is high, and at the fracture cross junction, due to the contraction effect of the gap width, the flow is diverted to a low-pressure area under the constraint of the wall. This diverted fluid collides with the low-velocity fluid occurring in the horizontal fracture, as shown in areas a and c in Figs. 11 and 12. Based on the streamline diagram, it is found that vortices are generated at the cross fractures, and the velocity vector diagram shows a complex disordered flow behavior, which is the mesoscopic impact of the seepage resistance effect in response to the abrupt change in gap width via contraction.

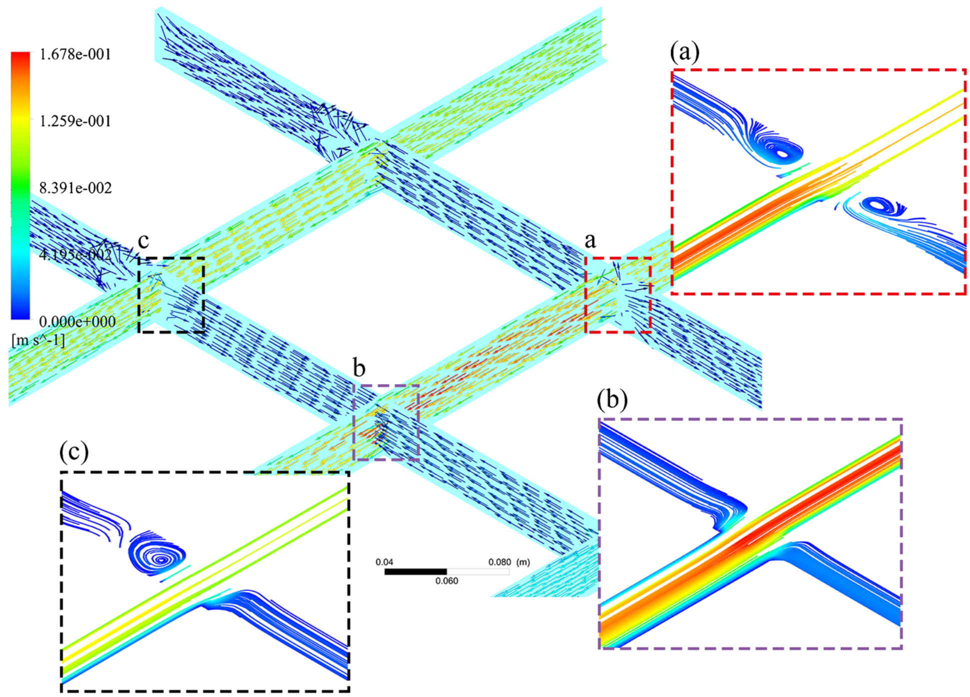


**Fig. 11** Velocity vector diagram and mesoscale streamline diagram of the quadrilateral fracture network: **a** frature gap width contraction zone, **b** frature gap width expansion zone, **c** frature gap width contraction zone

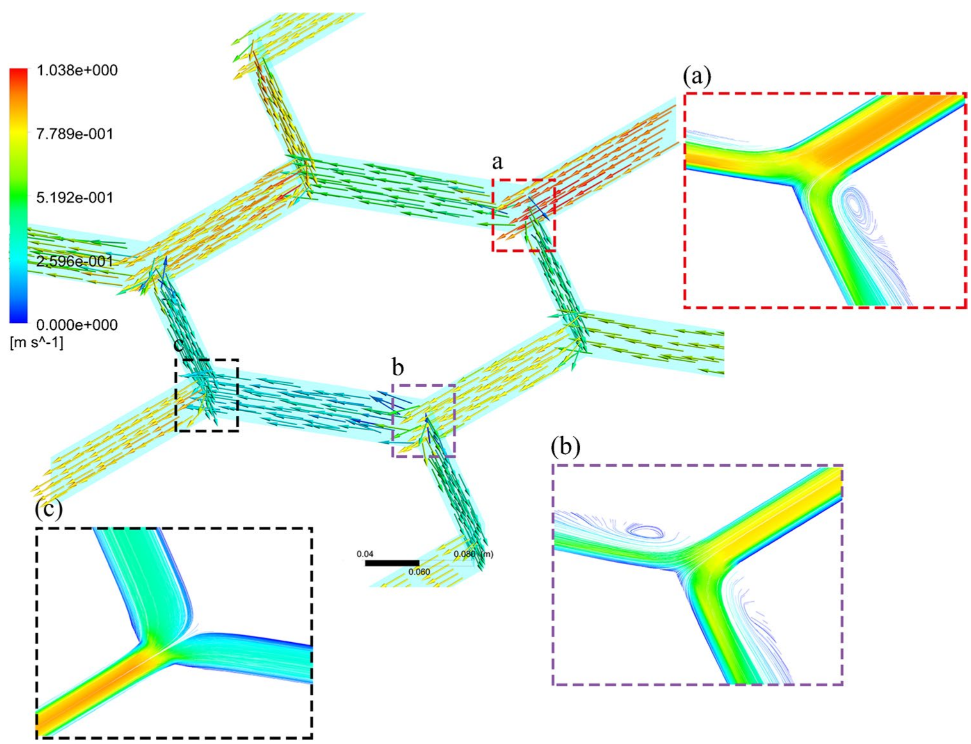


**Fig. 12** Velocity vector diagram and mesoscale streamline diagram of the hexagonal fracture network: **a** frature gap width contraction zone, **b** frature gap width contraction zone, **c** frature gap width expansion zone

Compared with the previous research results, the E-loss model proposed in this paper has a wider scope of application. The concept of equivalent seepage resistance is added to the research results of Zhu et al. Therefore, the complex flow diversion problem of fracture network can be transformed into the series parallel problem of resistance, which expands the application scope of this method; In the application of columnar jointed rock mass, if the change of equivalent seepage resistance caused by the change of fracture opening is ignored, the E-loss model will degenerate into the model proposed by Kong et al. In conclusion, the E-loss model is an improvement of the existing model, and can better reflect the seepage process of complex joint network represented by columnar jointed rock mass.

## Conclusion

To investigate the characteristics of nonlinear flow in fracture networks, three aspects of theoretical models, physical model tests and numerical simulations are studied in this paper.

1. An E-loss model which can be used to calculate the flow of each fracture in the fracture network is established, the physical meaning of the model is clear and the calculation process is simple.
2. The physical model test results show that the water pressure drop is highly nonlinear with the flow rate in the fracture networks. The fracture connection mode exerts an important influence on the fracture hydraulic characteristics, which leads to a greater inertial energy loss. The test results show that the E-loss model better reflects the flow diversion occurring in the fracture network under a small water pressure drop, and the calculated values of the model are in good agreement with the measured values. With increasing water pressure drop, the Forchheimer equation adequately describes the observed nonlinear flow behavior in the fracture networks.
3. The numerical simulation results reveal that the dominant flow effect is obvious in the two fracture networks. In response to a sudden decrease in fracture width in the fracture network, there is an obvious eddy current blocking effect. This effect is the external impact of the local loss resistance under mesoscale conditions, and the mesoscale water flow state is consistent with the analysis results of the theoretical model.

In seepage analysis of fractured rock mass engineering, attention should be paid to the influences of the fracture connection mode and nonlinear seepage on the fracture hydraulic characteristics. In addition, under the existing theory, because the nonlinear flow effect and local head loss effect are ignored, the water inflow predicted with the linear Darcy equation under a high water pressure at great buried depths may be overestimated.

**Funding** This research was funded by the Fundamental Research Funds for the Central Universities (No. B200203096) and the Postgraduate Research & Practice Innovation Program of Jiangsu Province (KYCX20_0451). This research was also funded by the National Natural Science Foundation of China (No. 41831278 and 51579081).

## Declarations

**Conflict of interest** The authors declare no competing interests.

## References

Baghbanan A, Jing L (2007) Hydraulic properties of fractured rock masses with correlated fracture length and aperture. Int J Rock Mech Min Sci 44:704–719. https://doi.org/10.1016/j.ijrmms.2006.11.001

Berkowitz B (2002) Characterizing flow and transport in fractured geological media: a review. Adv Water Resour 25(8):861–884. https://doi.org/10.1016/S0309-1708(02)00042-8

Chen SH, Feng XM, Isam S (2008) Numerical estimation of REV and permeability tensor for fractured rock masses by composite element method. Int J Numer Anal Meth Geomech 32(12):1459–1477. https://doi.org/10.1002/nag.679

Chen YF, Hong JM, Tang SL, Zhou CB (2016) Characterization of transient groundwater flow through a high arch dam foundation during reservoir impounding. J Rock Mech Geotech Eng 8(4):462–471. https://doi.org/10.1016/j.jrmge.2016.03.004

Cherubini C, Giasi CI, Pastore N (2012) Bench scale laboratory tests to analyze non-linear flow in fractured media. Hydrol Earth Syst Sci 16(8):2511–2522. https://doi.org/10.5194/hess-16-2511-2012

Hu YJ, Mao G, Cheng W, Zhang J (2005) Theoretical and experimental study on flow distribution at fracture intersections. J Hydraul Res 43(3):321–327. https://doi.org/10.1080/00221680509500126

Johnson J, Brown S, Stockman H (2006) Fluid flow and mixing in rough-walled fracture intersections. Journal of Geophysical Research Solid Earth 111(B12):B12206. https://doi.org/10.1029/2005JB004087

Klimczak C, Schultz RA, Parashar R, Reeves DM (2010) Cubic law with aperture-length correlation: implications for network scale fluid flow. J Hydrol 18(4):851–862. https://doi.org/10.1007/s10040-009-0572-6

Kong H, Wang L (2018) Seepage problems on fractured rock accompanying with mass loss during excavation in coal mines with karst collapse columns. Arab J Geosci 11:585. https://doi.org/10.1007/s12517-018-3881-z

Kong Y, Zhu ZD, Ruan HN (2018) Stress-seepage coupling characteristics of jointed rock mass under three principal stresses. Rock and Soil Mechanics 6:2008–2016 ((**in Chinese**))

Konzuk JS, Kueper BH (2004) Evaluation of cubic law based models describing single-phase flow through a rough-walled fracture. Water Resour Res 40(2):W02402. https://doi.org/10.1029/2003WR002356

Kulatilake P, Panda BB (2000) Effect of block size and joint geometry on jointed rock hydraulics and REV. J Eng Mech 126(8):850–858. https://doi.org/10.1061/(ASCE)0733-9399(2000)126:8(850)

Lam K, Gong WQ, So RMC (2008) Numerical simulation of cross-flow around four cylinders in-line square configuration. J Fluids Struct 24(1):34–57. https://doi.org/10.1016/j.jfluidstructs.2007.06.003
Li S, Zhang N, Li Q, Vadim S (2020) Stability study of fluid-solid coupled dynamic system of seepage in accumulative broken rock. Arab J Geosci 13:647. https://doi.org/10.1007/s12517-020-05559-5
Liu R, Jiang Y, Li B, Wang XS (2015) A fractal model for characterizing fluid flow in fractured rock masses based on randomly distributed rock fracture networks. Comput Geotech 65:45–55. https://doi.org/10.1016/j.compgeo.2014.11.004
Lomize GM (1951) Flow in fractured rock. Moscow, Russia, Gosemergoizdat, pp 127–129 ((**In Russian**))
Louis C (1969) A study of groundwater flow in jointed rock and its influence on the stability of rock masses (Rock Mech.Res.Rep.10). London, UK, Imperial College
Niu Z, Zhu Z, Que X (2020) Constitutive model of stress-dependent seepage in columnar jointed rock mass. Symmetry 12:160. https://doi.org/10.3390/sym12010160
Qian JZ, Zhan HB, Chen Z, Ye H (2011) Experimental study of solute transport under non-Darcian flow in a single fracture. J Hydrol 399(3):246–254. https://doi.org/10.1016/j.jhydrol.2005.01.013
Qiao LP, Wang ZC, Li SC, Bi LP, Xu ZH (2017) Assessing containment properties of underground oil storage caverns: methods and a case study. Geosci J 21(4):579–593. https://doi.org/10.1007/s12303-016-0063-4
Sang S, Liu WQ, Song L, Zhang T, Shen HD (2016) On the flow distribution characteristics of cross cracks in rock mass. Journal of Experimental Mechanics 31(5):577–583 ((**in Chinese**))
Scesi L, Gattinoni P (2007) Roughness control on hydraulic conductivity in fractured rocks. Hydrogeol J 15(2):201–211. https://doi.org/10.1007/s10040-006-0076-6
Shang X, Wang J, Zhang Z, Gao F (2019) A three-parameter permeability model for the cracking process of fractured rocks under temperature change and external loading. Int J Rock Mech Min Sci 123:104106. https://doi.org/10.1016/j.ijrmms.2019.104106
Skjetne E, Hansen A, Gudmundsson JS (1999) High-velocity flow in a rough fracture. J Fluid Mech 383:1–28. https://doi.org/10.1017/S0022112098002444
Su BY (1997) Zhan M L (1997) Experiment research of cross fracture flow. J Hydraul Eng 5:1–6 ((**in Chinese**))
Su GW, Geller JT, Pruess K, Feng W (1999) Experimental studies of water seepage and intermittent flow in unsaturated, rough-walled fractures. Water Resour Res 35(4):1019–1037. https://doi.org/10.1029/1998WR900127
Takahashi M, Park H, Takahashi N (2013) True triaxial tests-using permeability and extensional stress parameters to simulate geological history in rocks. Geosyst Eng 16:75–82
Tao Y, Liu WQ (2012) An equivalent seepage resistance model with seepage-stress coupling for fractured rock mass. Rock and Soil Mechanics 7:2041–2047 ((**in Chinese**))
Tian KM (1986) The hydraulic properties of crossing-flow in an intersected fracture. Acta Geol Sin 60(2):202–214 ((**in Chinese**))
Wang H, Xu W, Shao J (2014) Experimental researches on hydro-mechanical properties of altered rock under confining pressures. Rock Mech Rock Eng 47:485–493. https://doi.org/10.1007/s00603-013-0439-y
Wang P, Yang T, Xu T, Yu Q (2013) Liu H (2013) A review of critical conditions for the onset of nonlinear fluid flow in rock fractures. J Appl Math 8:361–376. https://doi.org/10.1155/2013/420536
Wang ZC, Li SC, Qiao LP, Zhang QS (2015) Finite element analysis of hydromechanical behavior of an underground crude oil storage facility in granite subject to cyclic loading during operation. Int J Rock Mech Min Sci 73:70–81. https://doi.org/10.1016/j.ijrmms.2014.09.018
Whitaker S (1996) The Forchheimer equation: a theoretical development. Transp Porous Media 25(1):27–61. https://doi.org/10.1007/BF00141261
Wu Q, Kulatilake P (2012) REV and its properties on fracture system and mechanical properties, and an orthotropic constitutive model for a jointed rock mass in a dam site in China. Comput Geotech 43:124–142. https://doi.org/10.1016/j.compgeo.2012.02.010
Yang T, Jia P, Shi W, Wang P, Liu H, Yu Q (2014) Seepage–stress coupled analysis on anisotropic characteristics of the fractured rock mass around roadway. Tunn Undergr Space Technol 43:11–19. https://doi.org/10.1016/j.tust.2014.03.005
Yu L, Liu R, Jiang Y (2017) A review of critical conditions for the onset of nonlinear fluid flow in rock fractures. Geofluids 2017:1–17. https://doi.org/10.1155/2017/2176932
Zhang W, Chen J-P, Liu C, Huang R, Li M, Zhang Y (2012) Determination of geometrical and structural representative volume elements at the Baihetan dam site. Rock Mech Rock Eng 45(3):409–419. https://doi.org/10.1007/s00603-011-0191-0
Zhang X, Guo X, Dai L, Liu J, Wang G (2021) Vibration characteristics of marine riser groups considering the coupled action of cross-flow and in-line. Arab J Geosci 14:226. https://doi.org/10.1007/s12517-021-06532-6
Zhu HG, Xie HP, Yi C, Jiang YD, Liu JX, Lai SL, Dong X (2013) Analysis of properties of fluid flow in rock fractures. Chin J Rock Mech Eng 32(4):657–663 ((**in Chinese**))
Zou L, Tarasov B, Dyskin AV, Adhikary D, Pasternak E, Xu W (2013) Physical modeling of stress-dependent permeability in fractured rocks. Rock Mech Rock Eng 46:67–81. https://doi.org/10.1007/s00603-012-0254-x